A miniaturised, nested-cylindrical electrostatic analyser geometry for dual electron and ion, multi-energy measurements.

Robert Bedington[1,*], Dhiren Kataria[*], Alan Smith[*]

University College London, Mullard Space Science Laboratory, Holmbury St. Mary, Dorking RH5 6NT.

Abstract

The CATS (Cylindrical And Tiny Spectrometer) electrostatic optics geometry features multiple nested cylindrical analysers to simultaneously measure multiple energies of electron and multiple energies of ion in a configuration that is targeted at miniaturisation and MEMS fabrication. In the prototyped model, two configurations of cylindrical analyser were used, featuring terminating sideplates that caused particle trajectories to either converge (C type) or diverge (D type) in the axial direction. Simulations show how these different electrode configurations affect the particle focussing and instrument parameters; C-type providing greater throughputs but D-type providing higher resolving powers. The simulations were additionally used to investigate unexpected plate spacing variations in the as-built model, revealing that the K-factors are most sensitive to the width of the inter-electrode spacing at its narrowest point.

Keywords: Plasma, Electrostatic analyzer, Micro-fabrication, SIMION

1. Introduction

In many fields of research, from space science to the analysis of surfaces, electrostatic analysers are used to measure the energies, and sometimes the masses,

*Corresponding author
URL: r.bedington@nus.edu.sg (Robert Bedington)
[1]Now at NUS Centre for Quantum Technologies, Singapore.

of electrons and ions (of a few eV to a few tens keV) by deflecting and focussing them with electrodes. A myriad of electrode designs exist to accomplish this, each optimised toward specific particle study requirements and environment restrictions. For many applications, the miniaturisation of electrodes is desirable, and so a number of MEMS (Micro Electro Mechanical Systems) based devices have been developed [1, 2, 3].

Some applications benefit from the simultaneous measurement of multiple energies of particle [4], and many space plasma measurements require both electron and (positive) ion data and so use two, oppositely configured analysers [5, 6].

To achieve multiple measurements in a smaller sized package, curved plate electro-static analysers like these can be nested within each other (like Russian dolls). The FESA [7], for example, uses nested top hat geometry electrostatic analysers to allow two E/Q (energy per charge) ratios of electron to be sampled simultaneously. AMPS [8] on the other hand, is a nested spherical geometry analyser that allows one energy of electron and one E/Q of ion to be sampled simultaneously.

The coaxially nested cylindrical geometry discussed in this paper builds on both of these developments, using ten levels of nesting to allow five different energies of negative E/Q (hereafter called electron energies) and five different positive E/Q (hereafter called ion energies) to be sampled simultaneously. It uses a cylindrical geometry for ease of manufacture at small scales.

The CATS electrostatic analyser design [9] was developed as a prototype study of this geometry. It is well-suited to micro-fabrication methods and was developed primarily for aerospace applications including space weather detectors for nanosatellites and high time resolution instruments for multipoint space physics studies [10, 11].

In this paper we explore some of the detail of the nested cylindrical geometry used in the CATS design. Specifically we use high-resolution, Monte-Carlo SIMION charged particle ray-tracing simulations to determine its ideal-world focussing properties and use electron-beam tests to show the impact to the

analyser response of real-world manufacturing deviations in the as-built model.

2. CATS Geometry

Figure 1 shows the CATS design; ten concentric 90° cylindrical electrostatic analysers (hereafter termed "channels"), arising from two contiguous electrodes (shown more clearly later in figure 3). The orange coloured sections are an electrically grounded electrode, the black coloured sections are an adjustable voltage electrode.

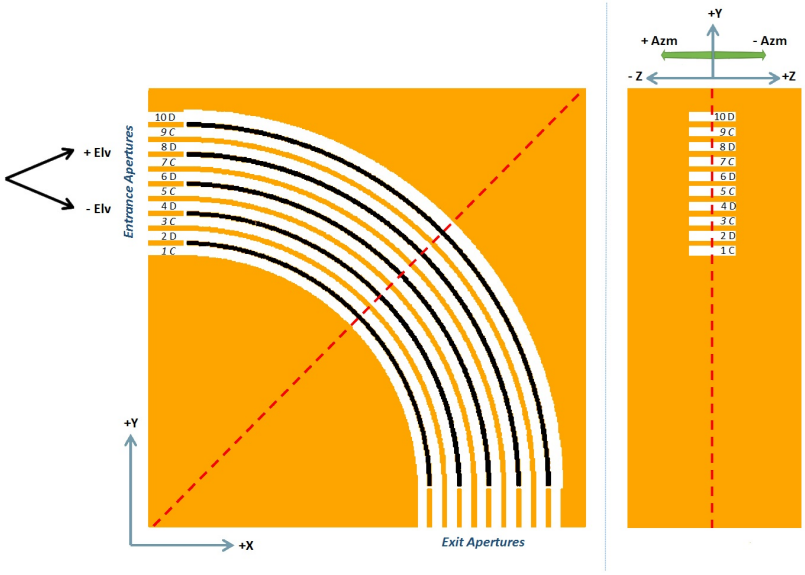

Figure 1: (Colour online). Left: Central cross-section schematic view of the CATS analyser design. Right: front view of CATS analyser design showing input (entrance) apertures. Orange indicates grounded electrode, black indicates electrode at analyser voltage, ($V_{applied}$). Dashed lines show lines of symmetry used to optimise simulations. Channel number labels and channel type (C or D – as explained in the text) are also indicated.

If a positive voltage is applied to the black electrode, then the channels suffixed 'D' will analyse electrons and the channels suffixed 'C' will analyse ions, and vice versa if the voltage is negative.

For any given voltage applied, the peak energy of particles transmitted by an individual ideal cylindrical analyser is determined by the k-factor, K, (some-

times called the plate factor) and is approximated by the following equation [12]:

$$K = \frac{E_{selected}}{V_{applied}} = \frac{1}{2\ln\frac{R_{outer}}{R_{inner}}} \approx \frac{R_0}{2 \times \Delta R} \tag{1}$$

Where $E_{selected}$ is the peak energy of the successfully transmitted particles (of unit charge), R_{outer} is the radius of the outer (larger) channel wall, R_{inner} is the radius of the inner channel wall, $V_{applied}$ is the potential difference between R_{inner} and R_{outer}, R_0 is the mean radius of curvature of the channel and ΔR is the channel width (R_{outer}-R_{inner}). The CATS ΔR and R_0 are shown in figure 2.
.

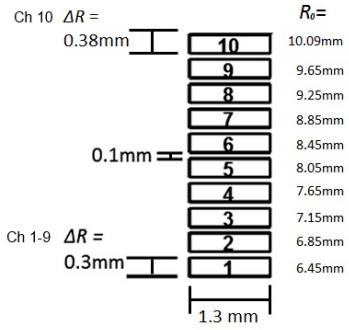

Figure 2: CATS apertures, showing aperture dimensions and key analyser dimensions (entrance and exit apertures are identical). As can be seen in figure 1, channel 10 has a larger ΔR due to an oversized R_{outer}, however its aperture size is the same as the other channels.

It can thus be seen that the peak energy analysed increases as the channel number (thus R_0) increases.

Equation 1 is only an approximation however since it is valid only where the field is directly perpendicular to the curved electrode plates and so does not account for the ends of the analyser: i.e. the x-y plane terminating plate electrodes in the plus and minus Z direction in figure 2. The full three-dimensional nature of the electrodes is shown in an exaggerated cutaway schematic view in figure 3, displaying the terminating end-plates that connect the black electrodes (construction details are shown in a previous publication [9]).

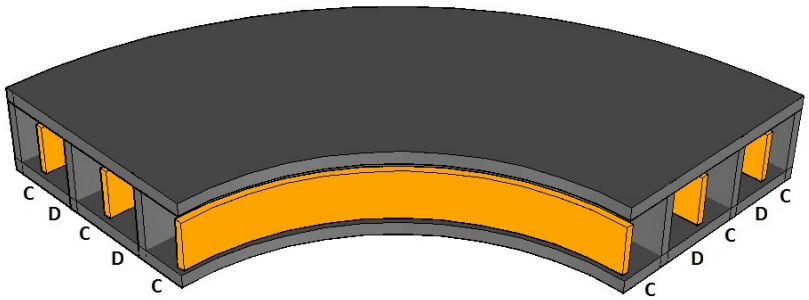

Figure 3: (Colour online). Cutaway schematic showing a (not to scale) section of the CATS analyser channels structure. The sections coloured in orange are electrically grounded, analyser voltage is applied to sections coloured in black creating C and D channels as marked. Structurally the electrically-grounded plates are held in position by electrically-grounded apertures at either end (not shown here but visible in figure 1).

It can be seen in this figure that both ends (top and bottom in this orientation) of the CATS channels plates for all channels are marked black, i.e. they are all contiguous with the black coloured electrode and thus are at the potential being applied to the device and not at ground. This means that with a negative applied voltage the ions would be attracted to the these terminating plates and the electrons repelled and vice versa for a positive applied potential. Said another way, the odd numbered ("C", converging) channels will always have an edge-field that concentrates particles towards the centre of the channel, and the even numbered ("D", diverging) channels will always have an edge field that attracts particles toward the terminating plates.

To model the charged particle optics of such arrangements, computer simulations were developed. In the following section these simulations will be used to show how the D and C-channel designs affect the instrument parameters and focussing properties of the CATS analyser.

3. Simulations

The SIMION 8 software package[13] was used to perform charged particle ray tracing simulations. These modelled the CATS geometry as a 3D construction of

6.25 µm length cubes and calculated the electric fields accordingly. Randomised particles were generated at the CATS entrance aperture, covering at least the full range of velocities that could be selected by the analyser, and their trajectories were calculated. For particles that successfully exited the analyser, the input parameters were recorded, and used to produce histograms of the energies, angles and positions of the incoming particles [14]. From these histograms, the k-factors, and the energy and angular resolutions were measured, in most cases using the terms of a Gaussian curve fitted to the histogram.

The geometric factor (the factor relating the number of particles transmitted through the analyser, N_{det}, to the differential directional number flux of the plasma) is calculated using the following equation:

$$G = \left(\frac{N_{detected}}{N_{in}}\right)(\Delta y \Delta z)\left(4\arcsin\left(\sin\frac{\Delta\theta}{2}\sin\frac{\Delta\phi}{2}\right)\right)\left(\frac{\Delta E}{E_{peak}}\right) \qquad (2)$$

For space plasma applications this is often quoted in the units of $\mathrm{cm}^2\,\mathrm{sr}\,\mathrm{eV}\,\mathrm{eV}^{-1}$. In this equation, N_{in} in is the total number of particles spawned (which must be large to minimise statistical uncertainty) and $\Delta y \Delta z$ is the area of the 2D plane in which they were spawned in cm^2 [which is $\geq$ to the entrance aperture]. $\Delta\theta$ and $\Delta\phi$ are the range of angles of the input (being greater than or equal to the angular acceptance of the instrument) and the trigonometric expression in which they appear describes the solid angle that the two orthogonal angles create. ΔE is the range of energies, and E_{peak} is the peak energy selected by the analyser for a given $V_{applied}$.

The Monte-Carlo simulations were continued at least until the statistical uncertainty in the extracted parameters due to the number of data points became insignificant compared to the uncertainty in the extracted parameter measurements (i.e. the uncertainties arising from a deviation from a true Gaussian response).

3.1. Instrument parameters

The instrument parameter results for each channel, as extracted from the simulation results, can be seen in figure 4.

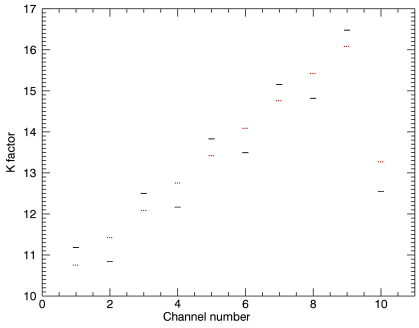

(a) K-factor variation with channel number, theoretical approximations shown with dotted lines (red online).

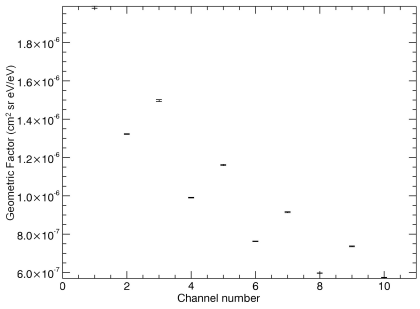

(b) Geometric factor variation with channel number.

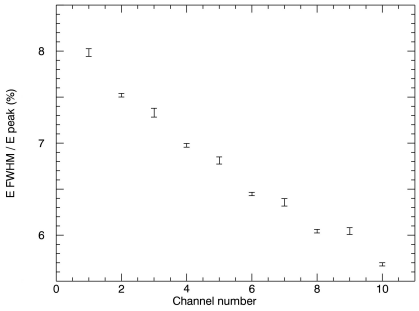

(c) Energy resolution (FWHM / E_{peak}) variation with channel number.

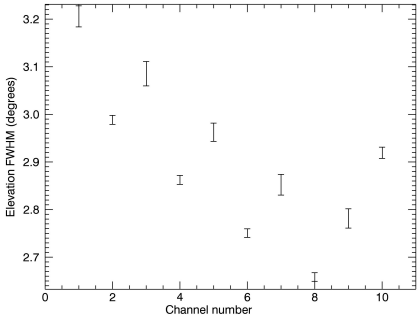

(d) Elevation FWHM variation with channel number.

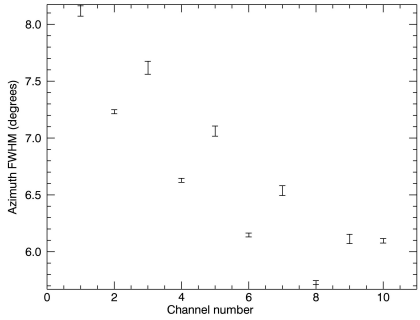

(e) Azimuth FWHM variation with channel number.

Figure 4: Instrument parameters extracted from the CATS SIMION simulations. Increasing channel number corresponds to increasing R_0. Even numbered channels are C-type, odd numbered channels are D-type. The error bars plotted reflect the uncertainties arising from the methods of curve-fitting to extract parameters from the histogrammed results (explained in the text).

Figure 4a shows the k-factors for the different channels in black, and the theoretical approximations (from equation 1) in red. It can be seen that the C-channel type (odd numbered channels) causes k-factors to be higher than the approximation, and that the D-channel type (even numbered channels) causes lower k-factors. The wider electrode gap (ΔR) for channel 10 causes a correspondingly reduced k-factor.

Figure 4b shows the geometric factors for the different channels. Unlike the k-factor this decreases with increasing R (as the path length of the channel increases while ΔR and the size of the apertures remain constant). Again the C-channels have a larger value than corresponding D-channels. This can be attributed to the focussing effect of the terminating end-walls, repelling all the particles inwards. The D-channels have the opposite effect, causing particles away from the centre to diverge, impact the walls and thus not be detected.

Since the apertures are the same size, the larger ΔR in channel 10 makes less difference here. The total geometric factor of all channels together is $1.05 \times 10^{-5}\,\mathrm{cm^2\,sr\,eV\,eV^{-1}}$.

The energy resolutions (FWHM / E_{peak}), shown in figure 4c, show little variation between C and D-channels. As the channels become longer, ΔR remains the same, so the bandpass of energies transmitted becomes smaller, and the energy resolution improves (decreases). The C-channels have a larger error bar as their energy response is further from an ideal Gaussian shape.

The angular resolutions of the channels, shown in figures 4d and 4e, follow a similar pattern to the geometric factors. The exception to this is channel 10, where the larger gap allows for an increase in the size of the azimuthal bandpass and a significant increase in the elevation bandpass. Again, the larger error bars are present on the C-channels due to their response deviating from an ideal Gaussian.

3.2. Focussing properties

The simulations logged the parameters of the randomised particles at the entrance and exit apertures of the analyser. To investigate the transmission

characteristics in more detail, the input parameters of the successfully transmitted particles were used to generate spectrogram-like 2D-histograms of the data. Figure 5 shows energy-elevation plots showing D channels and C-channels separately, and figure 6 likewise shows azimuth-energy plots.

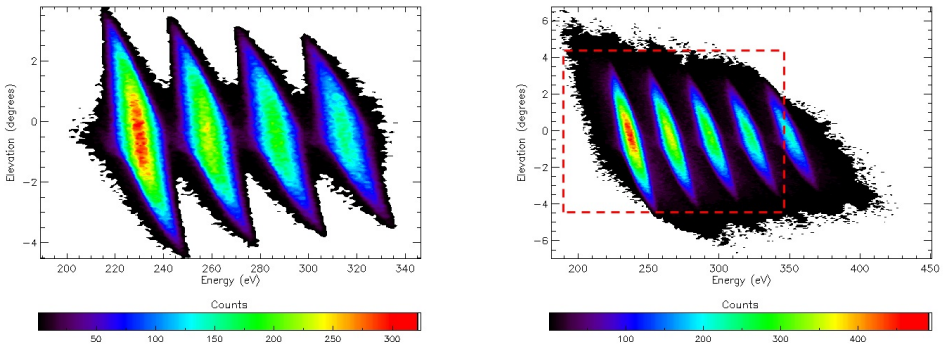

(a) D-channels; left to right 2,4,6,8.

(b) C-channels; left to right 1,3,5,7,9.

Figure 5: (Colour online). 2D histograms of input elevation angles and energies of detected simulation particles. For clarity channel 10 data has not been included, since it significantly overlaps in energy range with channel 4. Note the scales are different—the dashed box in (b) represents the size of the plot window of (a).

The diamond-like shape of the elevation response is typical of curved plate analysers [15], the stubby tail shape seen at low energies and central angles appears to be a slight artefact introduced by modelling the curved plate surfaces as a stepped construction of cubes. Simulations run using 12.5 µm and 25 µm length cubes had much more significant tails, but at 6.25 µm the resolution limits of the setup had been reached.

It can be seen that C-channels accept a much wider range of angles than the D-channels, most notably in azimuth. This is caused by the repulsive nature of the C-channel walls reflecting particles toward the centre of the channel in the +/- z direction. This behaviour can be inferred from figure 7 which shows 2D histograms of the azimuth angle of the incoming particles correlated with their positions along the z axis for both the entrance and exit apertures of the analyser.

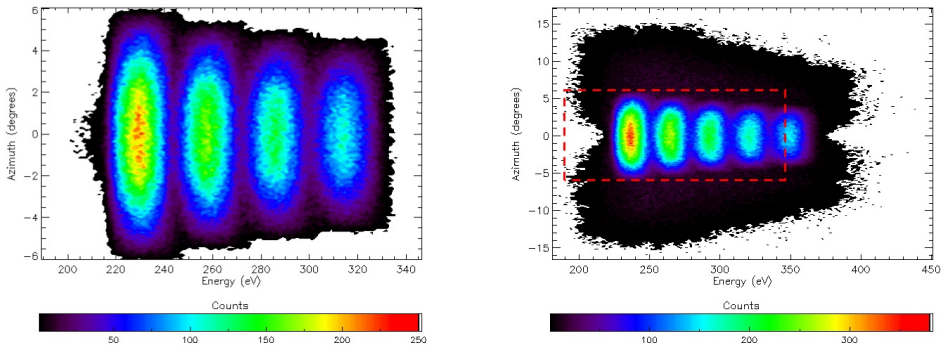

(a) D-channels; left to right 2,4,6,8.

(b) C-channels; left to right 1,3,5,7,9.

Figure 6: (Colour online). 2D histograms of input azimuth angles and energies of detected simulation particles. For clarity channel 10 data has not been included, since it significantly overlaps in energy range with channel 4. Note the scales are different—the dashed box in (b) represents the size of the plot window of (a).

For a D-channel, e.g. channel 8 in figure 7a and 7c, it can be seen that in general the widest azimuth particles enter at one end of the entrance aperture and exit from the opposite end (in the z direction). For example, the only possible paths for particles with azimuth angles greater than 4.5° are those entering at $z > +0.6$, and then exiting the analyser at $z < -0.6$.

For a C-channel, e.g. channel 9 in figures 7 (b) and (d), the azimuth response at central angles is similar to the D-channels. At wider angles however, thick dark bands can be seen in the figures that correspond to particles that have reflected off the terminating side-walls, resulting in the same shape response at the entrance and exit.

At the most extreme azimuths (>10° and <−10°) however, there are much fainter bands showing a handful of particles that have undergone two reflections off C-channel side walls, so (like the D channels and the unreflected particles found at central azimuths) their z distribution is also found to be reversed between entrance and exit.

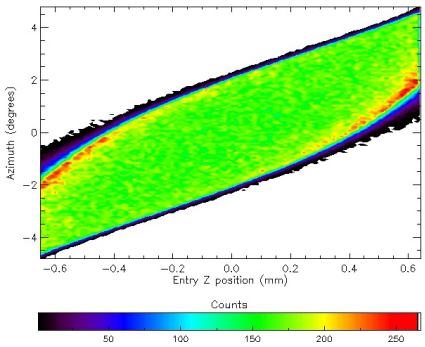

(a) Channel 8 (D) entrance Z position.

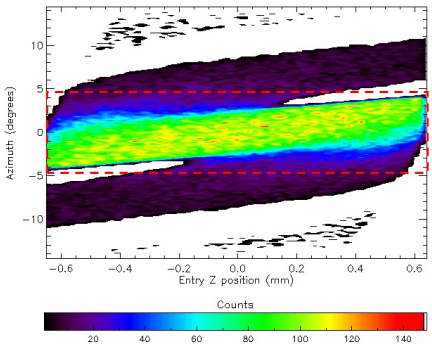

(b) Channel 9 (C) entrance Z position.

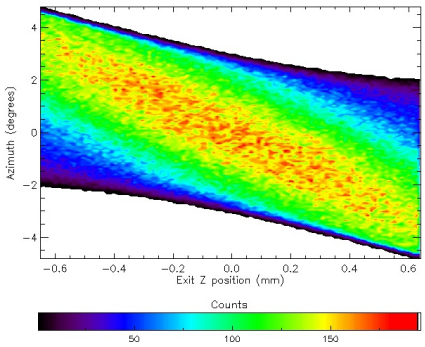

(c) Channel 8 (D) exit Z position.

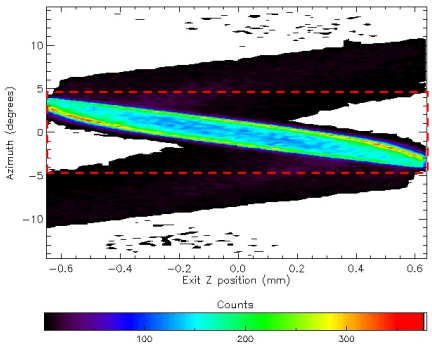

(d) Channel 9 (C) exit Z position.

Figure 7: (Colour online). 2D histograms of input azimuth angles and z positions (at CATS entrance and exit apertures, see figure 1) of detected simulation particles. Note the scales are different—the dashed box in (b) represents the size of the plot window of (a).

4. Experimental

As has been discussed elsewhere [9] an EDM (Electron Discharge Machining) prototype of the design was made and tested in an electron instrument calibration chamber. This prototype was found to feature some unintended variations in the channel widths (ΔR), which can be seen by close inspection of figure 8.

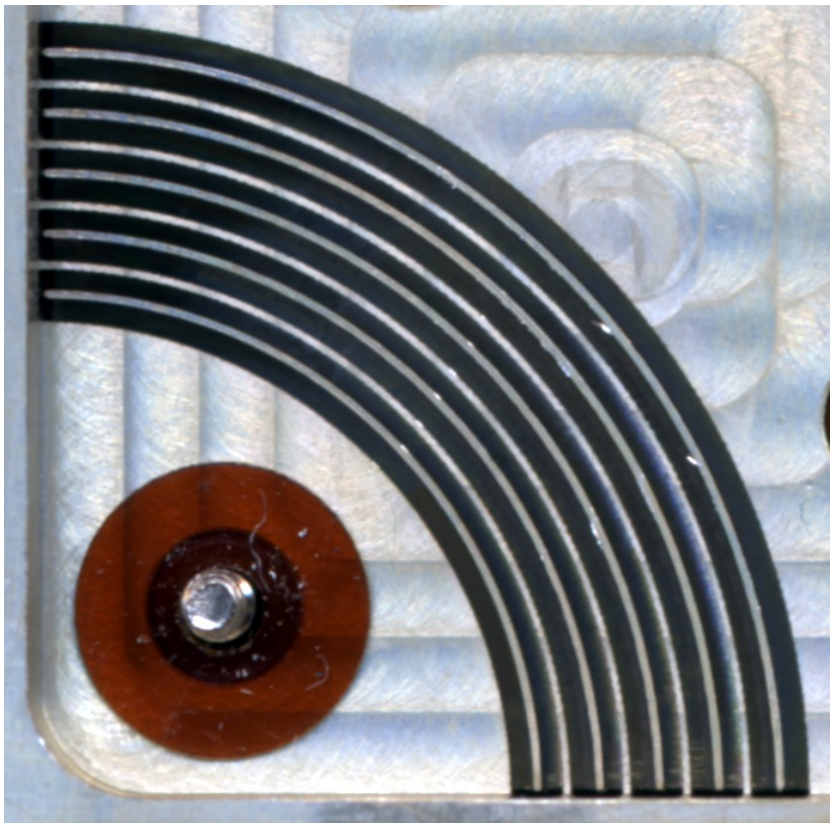

Figure 8: (Colour online). Flatbed scanner scan of CATS assembly post-testing. The ΔR gaps between channel electrodes (dark areas here) were designed to be uniform in spacing (except for channel 10, the largest). In this enlarged image however it can be seen that ΔR varies between channels, and along the length of individual channels. The flecks of swarf visible appear not to have affected the results.

The CATS entrance apertures were mounted on a two-axis rotation stage at the centre of a wide-area electron beam. At different times a CEM (Channel

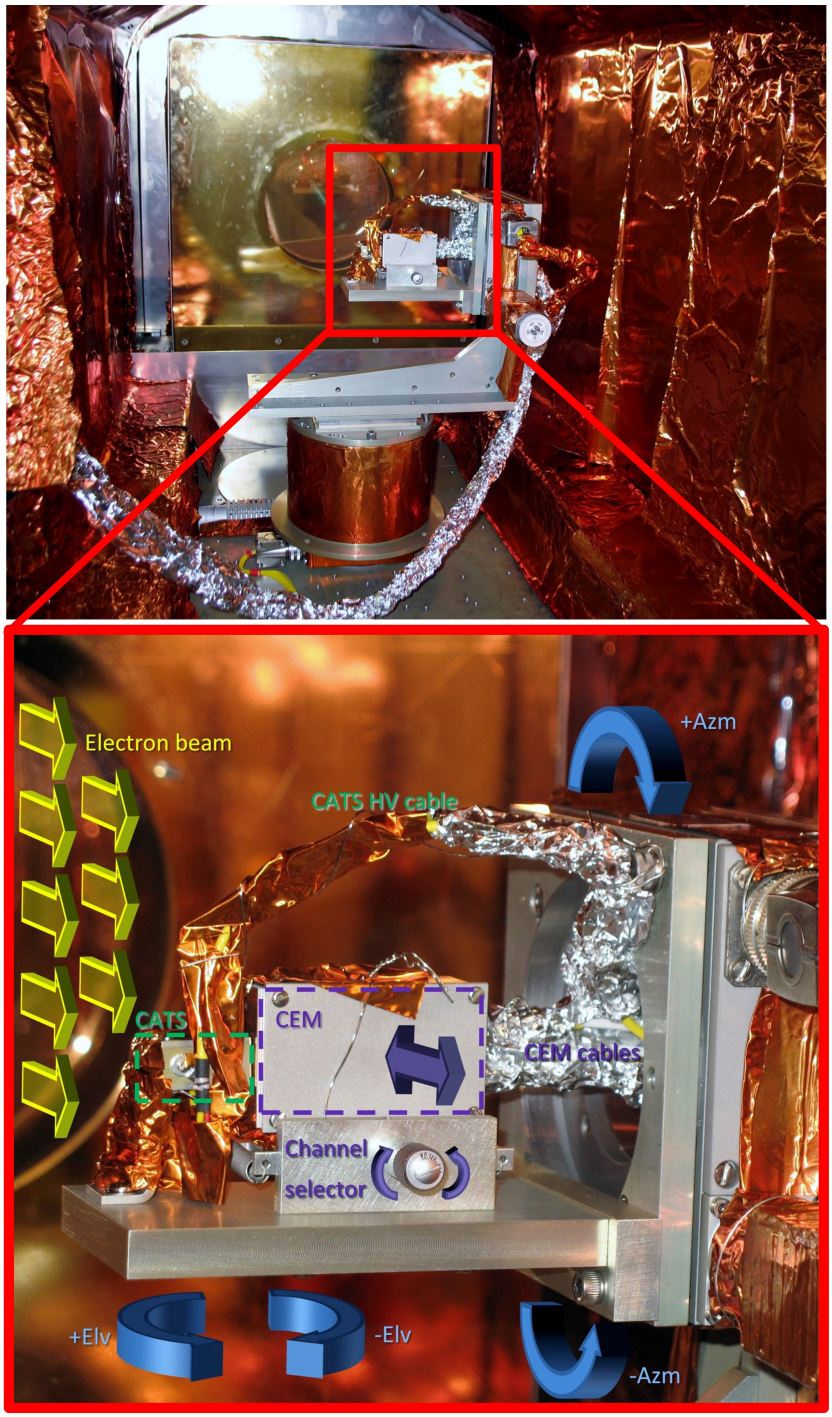

Figure 9: (Colour online). CATS+CEM vacuum chamber and electron beam testing setup. CATS and the CEM are mounted on a two-axis motorised rotation stage with the CATS entrance apertures at the point orthogonal to the two rotation axes and the centre of the beam. By turning the 'channel selector' control, the collimated entrance aperture of the CEM can be moved forwards and backwards to position it at the exit apertures of different CATS channels. Grounded foil coverings are used to prevent insulated surfaces becoming charged and interfering with the electron beam.

Electron Multiplier) and a ion-implanted CCD [16] were used to detect electrons exiting CATS.

The electron beam calibration facility is shown in figure 9 and described in detail in [16, 17]. Figure 10 shows the peak k-factors for each channel as determined from these tests and compares them to the simulated k-factors from section 3.1.

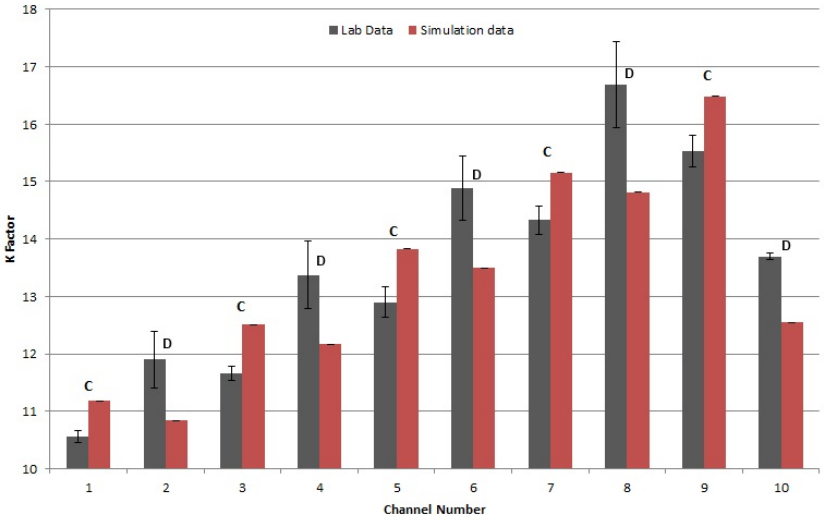

Figure 10: (Colour online). Comparison of the peak k-factors determined from simulations of the as-designed CATS (red) and CEM/CCD experimental measurements of the peak k-factors of the as-built CATS (black). Error bars on simulation results are as discussed in section 3.1, error bars on experimental results are based on averages from different tests.

This shows that the C-channels all have lower k-factors than the simulation, whereas the D-channels all have higher k-factors. From equation 1 we know that such changes can be caused by a change in R_0 or ΔR. If R_0 is assumed to be nominal, and the k-factor variations are caused by variations in ΔR alone, then they can be determined by equation 3:

$$\Delta R_{inf} = \Delta R_{sim} \times \frac{K_{lab}}{K_{sim}} \tag{3}$$

where ΔR_{inf} is the channel width that is being inferred from K_{lab}, the laboratory measured k-factor and ΔR_{sim} and K_{sim} are the simulated (design specifi-

cation) channel width and simulation measured k-factor respectively.

A close examination of Figure 8 reveals however that the channel widths in the as-built CATS vary not only channel-to-channel but also along their length, i.e. for every channel there is not a single value of ΔR. Accordingly five ΔR were measured for each channel, at regular intervals. Figure 11 shows three columns for each channel which compare: the difference between ΔR_{sim} and the average of the five ΔR measurements (green); the difference between ΔR_{sim} and the narrowest of these five measurements (blue); and the difference between ΔR_{sim} and ΔR_{inf} (brown).

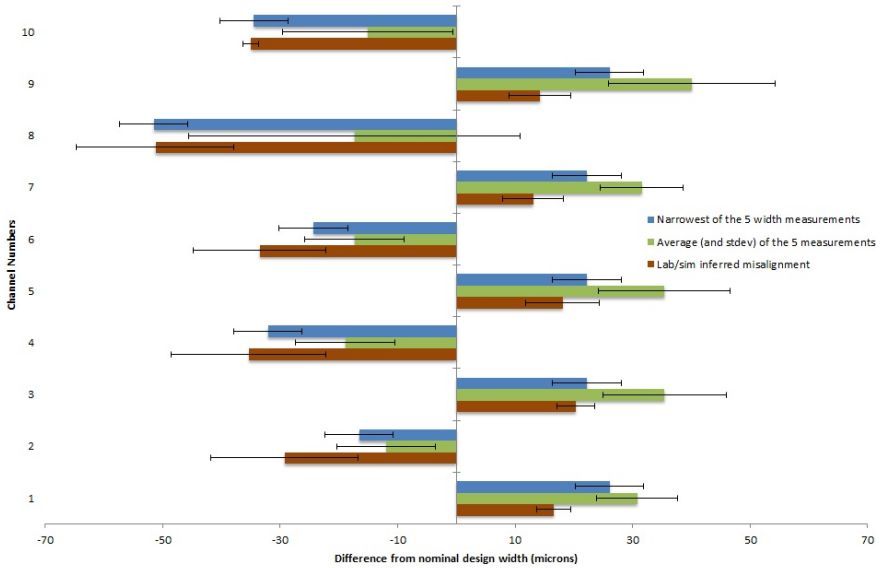

Figure 11: (Colour online). Comparison of the difference from ΔR_{sim} (nominal ΔR) as inferred from the k-factor difference (using equation 3) and as measured from figure 8. C-channels all have larger than nominal ΔR (+) and C-channels all have narrower than nominal ΔR (-).

Since the ΔR_{inf}-based values (brown bars) are in closest agreement with the narrowest measurements (blue bars), it would seem that the size of the narrowest gap is having the largest influence on the k-factor.

The azimuthal response was found to be largely as simulated (figure 12) suggesting that the electric fields parallel to the cylindrical axis of the analyser

plates were nominal.

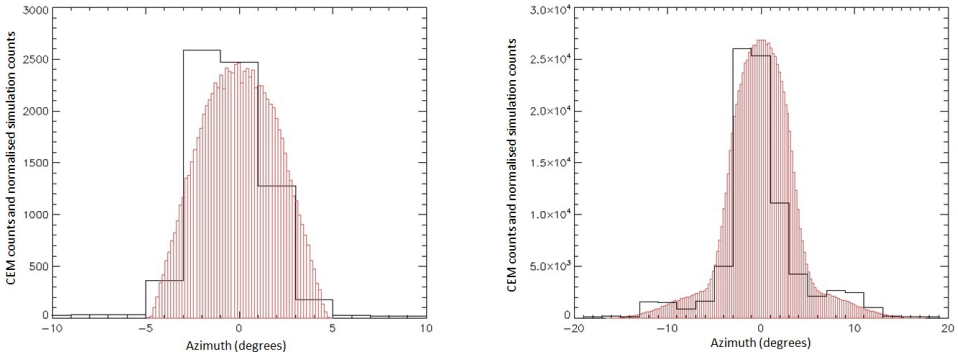

(a) D-channel 8.

(b) C-channels 7 and 9 combined.

Figure 12: (Colour online). Azimuth responses for 300eV electron beam. Black lines - CEM data summed over available CATS voltages and elevation angles. Red columns - corresponding simulation data. Data approximately normalised by curve height.

The elevation response however was not as simulated; C-channel peak elevations were slightly more positive than expected, and D-channel peak elevations more negative than expected (see figure 13). The elevation resolutions were also found to vary unexpectedly.

While experimental effects such as miscalibration and geomagnetic field interference could change the absolute values of the peak elevations, the relative difference between C and D channel peak elevation results could only realistically be explained by an irregularity in the electrode construction.

Further SIMION simulations showed that elevation angle peak offsets could be caused by misalignments in the concentricity of the analyser plates (i.e. outer and inner plates not being co-axial) but such misalignments were not found to be present in CATS in the visual data (such as figure 8) and the exact cause of this offset effect is at present unknown.

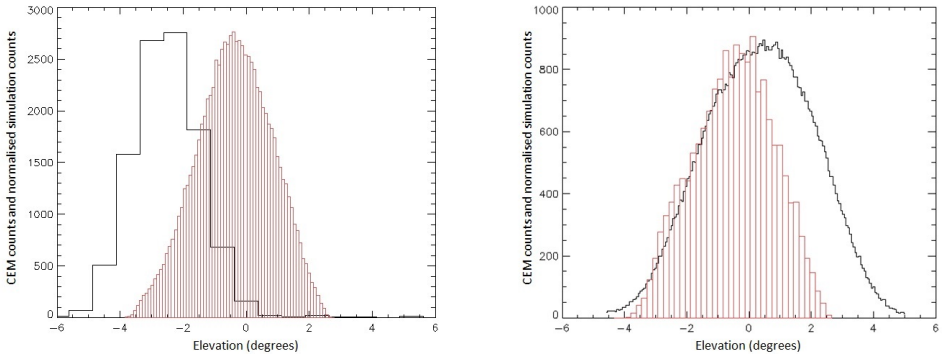

(a) D-channel 8.

(b) C-channels 7 and 9 combined. Laboratory data taken in high resolution.

Figure 13: (Colour online). Elevation responses for 300eV electron beam. Black lines - CEM data summed over available CATS voltages and elevation angles. Red columns - corresponding simulation data. Data approximately normalised by curve height.

5. Conclusions

It has been shown that for the CATS analyser geometry that due to the reflective nature of the electrode end-plates, the C-channels transmit more particles than the D-channels. It has been shown also that the angular resolutions and energy resolutions of the C-channels are consequently worsened. Depending on the manufacturing technique used, it is possible that an analyser might most easily be made with just C-channels, just D-channels or a CATS-like combination of C and D-channels. If angular collimators are fitted to the entrance apertures however, the widest angle trajectories could be blocked out and the C and D-channel responses would thus be largely similar.

From the experimental results we have seen that the k-factor is closely correlated with the narrowest gap, and that the elevation response can be complex. This work has also highlighted how EDM components should be carefully inspected for accuracy and methods to verify the alignment of components should be considered from the design stage. That said, it should be noted that CATS is a completely functional, entirely usable analyser and so was used for Pole-

CATS student sounding rocket mission[18] and for continuing laboratory-based experiments.

While the CATS design presented here was not targeted at any specific mission or space plasma population, different instrument parameters can be obtained by varying the dimensions to suit.

Acknowledgements

CATS Technology development funded by STFC rolling grant. R. Bedington CATS Ph.D. studentship [19] funded by STFC CASE with Astrium UK. This paper was written whilst at ISAS JAXA and thus partly supported by JSPS Grant-in-Aid for JSPS Fellows Grant Number 24.02792. Thanks to Yoshifumi Saito for his suggestions.

References

[1] R. Stalder, S. Boumsellek, T. Van Zandt, T. Kenny, M. Hecht, F. Grunthaner, Micromachined array of electrostatic energy analyzers for charged particles, J. Vac. Sci. Technol. A Vacuum, Surfaces, Film. 12 (4) (1994) 2554–2558.
URL http://ieeexplore.ieee.org/xpls/abs_all.jsp?arnumber=4929704

[2] D. M. Wesolek, F. A. Hererro, R. Osiander, M. A. G. Darrin, Design, fabrication, and performance of a micromachined plasma spectrometer, J. Microlithogr. Microfabr. Microsystems 4 (4) (2005) 041403. doi:10.1117/1.2114767.
URL http://link.aip.org/link/JMMMGF/v4/i4/p041403/s1&Agg=doi

[3] E. Wapelhorst, J. Hauschild, J. Muller, Complex MEMS: a fully integrated TOF micro mass spectrometer, Sensors Actuators A Phys. 138 (1) (2007) 22–27. doi:10.1016/j.sna.2007.04.041.

URL http://linkinghub.elsevier.com/retrieve/pii/S092442470700324X

[4] D. Cubric, A. De Fanis, I. Konishi, S. Kumashiro, Parallel acquisition electrostatic electron energy analyzers for high throughput nano-analysis, Nucl. Instruments Methods Phys. Res. Sect. A Accel. Spectrometers, Detect. Assoc. Equip. 645 (1) (2011) 227–233. doi:10.1016/j.nima.2010.12.055.
URL http://linkinghub.elsevier.com/retrieve/pii/S0168900210027968

[5] J. L. Burch, R. Goldstein, T. E. Cravens, W. C. Gibson, R. N. Lundin, C. J. Pollock, J. D. Winningham, D. T. Young, RPC-IES: The Ion and Electron Sensor of the Rosetta Plasma Consortium, Space Sci. Rev. 128 (1-4) (2006) 697–712. doi:10.1007/s11214-006-9002-4.
URL http://www.springerlink.com/index/10.1007/s11214-006-9002-4

[6] O. Norberg, J. Winningham, The MEDUSA electron and ion spectrometer and the PIA ultraviolet photometers on Astrid-2, Annales (2001) 593–600.
URL http://hal.archives-ouvertes.fr/hal-00316854/

[7] Y. Saito, S. Sasaki, M. Fujimoto, K. Maezawa, I. Shinohara, Y. Tsuda, H. Kojima, M. Hirahara, Y. Miyoshi, N. Terada, T. Mukai, High time resolution electron measurement by Fast Electron energy Spectrum Analyzer (FESA), AIP Conf. Proc. 53 (2009) 53–58. doi:10.1063/1.3169304.
URL http://link.aip.org/link/APCPCS/v1144/i1/p53/s1&Agg=doi

[8] H. O. Funsten, D. J. McComas, Limited resource plasma analyzers : Miniaturization concepts, in: Geophys. Monogr., Vol. 102, American Geophysical Union, 1998, pp. 157–167.
URL http://cat.inist.fr/?aModele=afficheN&cpsidt=2398880

[9] R. Bedington, D. O. Kataria, A. Smith, A highly miniaturized electron and ion energy spectrometer prototype for the rapid analysis of space plasmas.,

Rev. Sci. Instrum. 85 (2) (2014) 023305. doi:10.1063/1.4865842.
URL http://scitation.aip.org/content/aip/journal/rsi/85/2/10.1063/1.4865842http://www.ncbi.nlm.nih.gov/pubmed/24593352

[10] S. Eckersley, R. Wall, S. J. Schwartz, M. Pudney, R. Bedington, A nanosatellite multi-scale mission concept, enabled by highly miniaturised plasma physics payloads, Proc. Symp. Small Satell. Syst. Serv. P (5) (2010) 7.

[11] J. Fennell, H. Spence, T. Moore, J. Galloway, Magnetospheric Constellation Missions, in: Clust. Work. Multiscale/Multipoint Plasma Meas., Vol. 449, 2000, p. 235.
URL http://adsabs.harvard.edu/full/2000ESASP.449..235F

[12] A. D. Johnstone, The Geometric Factor of a Cylindrical Plate Electrostatic Analyzer, Rev. Sci. Instrum. 43 (7) (1972) 1030. doi:10.1063/1.1685826.
URL http://link.aip.org/link/?RSI/43/1030/1&Agg=doi

[13] D. J. Manura, D. A. Dahl, SIMION.
URL http://simion.com/

[14] R. Bedington, D. O. Kataria, A. Smith, S. Eckersley, Development of a highly miniaturised low resource plasma analyser suitable for small satellite applications, in: Proc. Symp. Small Satell. Syst. Serv., Vol. 18, ESA, Funchal, 2010.

[15] G. C. Theodoridis, Charged Particle Transmission through Cylindrical Plate Electrostatic Analyzers, Rev. Sci. Instrum. 39 (3) (1968) 326. doi:10.1063/1.1683362.
URL http://link.aip.org/link/?RSI/39/326/1&Agg=doi

[16] R. Bedington, D. Kataria, D. Walton, Using a CCD for the direct detection of electrons in a low energy space plasma spectrometer, J. Instrum. 7 (01) (2012) C01079–C01079. doi:10.1088/1748-0221/7/01/C01079.

URL http://stacks.iop.org/1748-0221/7/i=01/a=C01079?key=crossref.e39da030308c6f3bcf920a2f602e8801

[17] G. Lewis, C. Arridge, D. Linder, L. Gilbert, D. Kataria, A. Coates, A. Persoon, G. Collinson, N. André, P. Schippers, J. Wahlund, M. Morooka, G. Jones, A. Rymer, D. Young, D. Mitchell, A. Lagg, S. Livi, The calibration of the CassiniHuygens CAPS Electron Spectrometer, Planet. Space Sci. 58 (3) (2010) 427–436. doi:10.1016/j.pss.2009.11.008.
URL http://linkinghub.elsevier.com/retrieve/pii/S0032063309003535

[18] A. Lee, R. Bedington, Polecats-a plasma instrumentation technology demonstration for REXUS-14, in: L. Ouwehand (Ed.), 1st ESA Symp. Eur. Rocket Balloon Program. Relat. Res., ESA Communications, Thun, Switzerland, 2013, pp. 469–472.
URL http://opus.bath.ac.uk/38664/

[19] R. Bedington, A prototype Cylindrical And Tiny Spectrometer for the rapid energy analysis of space plasmas, Doctoral, University College London (2012).
URL http://discovery.ucl.ac.uk/1370609/